Available online at www.sciencedirect.com

ScienceDirect

Journal of Magnesium and Alloys 10 (2022) 689–696

www.elsevier.com/locate/jma

Full Length Article

Phase equilibria and microstructure investigation of Mg-Gd-Y-Zn alloy system

Janet M. Meier[a], Jiashi Miao[a], Song-Mao Liang[b], Jun Zhu[b], Chuan Zhang[b], Josh Caris[c], Alan A. Luo[a,d,*]

[a] *Department of Materials Science and Engineering, The Ohio State University, Columbus, OH 43210, USA*
[b] *CompuTherm LLC, Middleton, WI 53562 USA*
[c] *Terves LLC, Euclid, OH 44117, USA*
[d] *Department of Integrated Systems Engineering, The Ohio State University, Columbus, OH 43210, USA*

Received 6 August 2021; received in revised form 14 September 2021; accepted 29 September 2021
Available online 2 December 2021

Abstract

In order to develop high strength Mg-Gd-Y-Zn alloys, key experiments coupled with CALPHAD (CALculation of PHAse Diagrams) calculations were carried out in the current work to provide critical understanding of this important alloy system. Three Mg-10Gd-xY-yZn ($x = 4$ or 5, $y = 3$ or 5, wt.%) were mapped on Mg-Gd-Y-Zn phase diagrams for phase equilibria and microstructure investigation. Electron microscopy was performed for phase identification and phase fraction determination in as-cast and solution treated conditions. In all three alloys, the major phases were Mg-matrix and long period stacking order (LPSO) 14H phase. With ST at 400 and 500 °C, the phase fraction of LPSO 14H increased, particularly the fine lamellar morphology in the Mg matrix. The as-cast and 400 °C Mg10Gd5Y3Zn samples had Mg_5(Gd,Y) present. At 500 °C, Mg_5(Gd,Y) is not stable and transforms into LPSO 14H. The Mg10Gd5Y5Zn alloy included the W-Phase, which showed a reduction in phase fraction with solution treatment. These experimental results were used to validate and improve the thermodynamic database of the Mg-Gd-Y-Zn system. Thermodynamic calculations using the improved database can well describe the available experimental results and make accurate predictions to guide the development of promising high-strength Mg-Gd-Y-Zn alloys.

Keywords: Long period stacking order (LPSO); Microstructure; Magnesium alloys; CALPHAD; Alloy development.

1. Introduction

The effects of rare earth (RE) elements on the microstructure and mechanical properties of Mg alloys have been extensively investigated [1,2]. Of these effects, the formation of long period stacking ordered (LPSO) phases has provided an interesting avenue for designing new alloys for lightweight, high strength applications [1,3,4]. LPSO phases form in Mg alloys containing a transition metal (TM) with a smaller atomic radius than Mg, such as Zn; and RE elements with larger atomic radii, such as Y and Gd. The LPSO phase structure is typically composed of alternating hexagonal close packed (HCP) Mg layers and RE/TM-enriched face centered cubic (FCC) layers [3,5,6]. The RE and TM atoms cluster along the basal plane to form enriched layers and result in a reduction in the stacking fault energy for the lattice. The enrichment of these layers produces a stacking fault with local FCC lattice, which is a building block for the LPSO structure [7]. The type of LPSO structure that forms depends on the number of HCP Mg layers sandwiched between these building blocks. The most common LPSO phases, 14H and 18R, have three and two Mg layers, respectively, between the building blocks [5,7]. The morphology and type of the LPSO phase depend on the composition and thermomechanical processing of Mg alloys [8–15]. Two predominant morphologies are observed in most alloys: a blocky morphology (18R or 14H) at

* Corresponding author at: Department of Materials Science and Engineering, The Ohio State University, Columbus, OH 43210, USA.
E-mail address: luo.445@osu.edu (A.A. Luo).

https://doi.org/10.1016/j.jma.2021.09.019

the grain boundaries usually formed during solidification and a fine lamellar morphology (14H) extending through the Mg matrix usually formed during subsequent heat treatment.

In addition to the LPSO phases discussed above, there are several other phases observed in the Mg-Gd-Y-Zn alloy system. The first is Mg_5Gd, the equilibrium β-phase that forms as part of a well-studied precipitation sequence for Mg-Gd system [5,9,14,16–18]. The metastable precursor phases in the β precipitation sequence have been observed at the grain boundaries or, with sufficient Gd content, as fine precipitates in $\boldsymbol{\alpha}$-Mg grains [1,19–21]. One of the precursor phases in this sequence, β_1, is Mg_3RE. This phase has the same Heusler structure type as the W-phase ($Mg_3Y_2Zn_3$) [22,23], which has led to some confusion in proper identification and differentiation of these two phases in literature. Both Mg_3RE and the W-phase have a $Fm\bar{3}m$ structure with the RE atoms occupying the 4a sites and Mg atoms occupying the 4b sites [10,14,24]. The difference between the phases comes from the occupancy of the 8c sites. Mg_3RE primarily has the 8c occupied by Mg atoms, while the W-phase has (Mg+Zn) atoms occupying the 8c sites with a ratio of 1:3 [14,25]. Both phases have some solid solubility of Zn and some REs, so the W-phase may be a subset of the Mg_3RE phase solid solubility region. Thus, more investigation is needed to clarify these phases in Mg alloys.

The W-phase is of interest because it is brittle and has limited adhesive strength with the Mg matrix [14,26]. Thus, it does not provide strengthening in cast alloys and can serve as a stress concentration site upon loading. The W-phase has been observed to start dissolving or transforming with solution treatment (ST) [14,27]. Mg_3RE has not been reported to provide much strengthening, but it has also not been reported to exhibit the same stress concentration effects as the W-phase. Mg_3RE has been reported to transform into the LPSO 14H and Mg_5RE with solution treatment [10,16,21,24,28]. It is unclear if the W-phase transforms into the LPSO 14H phase or dissolves into Mg solution. No observations of the transformation of the W-phase into Mg_5RE have been reported. Gröbner et al. reported both the W-phase and Mg_3RE to be present in an $Mg_{60}Gd_{20}Zn_{20}$ (at%) alloy [24]. The W-phase and Mg_3RE present a different morphology and z-contrast from each other in scanning electron microscopy [24]. Typically, the W-phase exhibits a fishbone-like or eutectic morphology and Mg_3RE has a blocky or globular morphology (when not in fine precipitate form) [10,14,16,24,26,27,29,30].

In a previous paper [31], two available CALPHAD (CALculation of PHAse Diagrams) software packages, Thermo-Calc (with TCMG5 database) and Pandat (with PanMg 2021 database), were used to investigate the phase equilibria and microstructure of three Mg-Gd-Y-Zn alloys. The predicted phases were generally consistent with those observed in the samples, but the predicted phase fractions were not always consistent with experimental results. Particularly, the LPSO 14H phase fraction predictions differed from experiments by $>$ 20 vol% in some cases. This discrepancy may come from either experimental uncertainty or inaccurate thermodynamic simulation. Therefore, it is necessary to obtain more reliable experimental data and further improve thermodynamic description of the Mg-G-Y-Zn system at the Mg-rich region.

Table 1
Composition of the three alloys used in this study (determined using ICP and OES).

Alloy	Mg (wt.%)	Gd (wt.%)	Y (wt.%)	Zn (wt.%)
Mg10Gd4Y3Zn	82.98	10.4	3.62	3.00
Mg10Gd5Y3Zn	81.73	10.57	5.25	2.45
Mg10Gd5Y5Zn	79.95	10.2	4.74	5.1

In this work, we investigate the as-cast and heat-treated microstructures of three Mg-Gd-Y-Zn alloys with electron microscopy. The experimental results are then used to improve the CALPHAD calculations of LPSO 14H and other phases in the alloy system. This research will provide fundamental understanding in phase equilibria and microstructure for alloy development in this critical alloy system.

2. Experimental methods and thermodynamic modeling

Three alloy compositions, as shown in Table 1 and designated as Mg10Gd4Y3Zn, Mg10Gd5Y3Zn and Mg10Gd5Y5Zn, were prepared using commercially pure Mg, Zn, Gd, and Y in a 34 kg (75 lb)-capacity furnace with a pneumatic shear mixer. The alloy compositions were initially selected in an attempt to maximize the LPSO 14H phase fraction in a critical region of the Mg-Gd-Y-Zn phase diagram with promising mechanical properties. When discrepancies were found between the CALPHAD prediction and experimentally measured phase fractions, the solution treatment temperatures were selected to clearly differentiate to phase regions in which each alloy composition existed and confirm phase stability. These alloys were used to provide experimental data to improve thermodynamic models in the system for phase equilibria calculations.

Each composition was cast into a steel permanent mold to make 18 x 18 x 10 cm (7″x7”x4”) plates which were sectioned for testing and analysis. Alloy chemistry (Table 1) was determined through a combination of inductively coupled plasma (ICP) and optical emission spectroscopy (OES) techniques. As-cast samples were mounted in Bakelite. Additionally, samples were vacuum encapsulated in borosilicate glass, solution treated (ST) at 400 and 500 °C for 24 h in a box furnace, water quenched, and subsequently mounted in epoxy for scanning electron microscope (SEM) analysis. An additional Mg10Gd5Y5Zn sample was ST at 500 °C for 24 h followed by another 24 h at 400 °C.

Samples were polished following standard metallography procedures up to 0.05 μm colloidal silica. SEM analysis was performed using a FEI Apreo FEG microscope with EDAX Octane Elect energy dispersive spectroscopy (EDS) capabilities. EDS spot and mapping analysis was performed using TEAM software at 15 kV and 1.6 nA. Area fraction analysis was performed using 10 SEM images, collected at 10 kV and 500x from each sample, using ImageJ software. The phase fraction measurements obtained from this method are

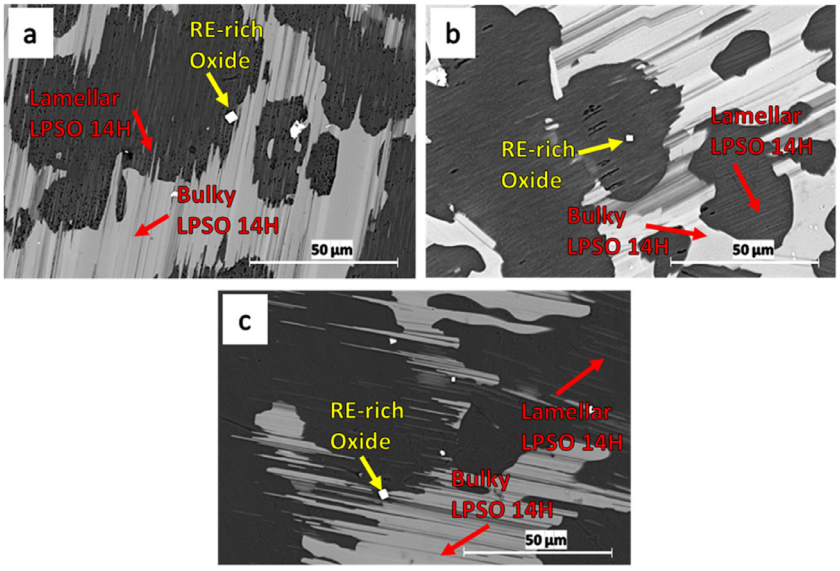

Fig. 1. SEM backscatter electron images of the Mg10Gd4Y3Zn composition in the (a) as cast, (b) solution treated at 400 °C 24 h, and (c) solution treated at 500 °C 24 h conditions. Examples of the blocky and lamellar LPSO phase are labeled with red arrows and the RE-rich oxide are labeled in yellow (For interpretation of the references to color in this figure legend, the reader is referred to the web version of this article).

in area%, but can be approximated as vol% based on the quantitative metallography standards established by Delesse [32]. The relatively uniform nature of bulk microstructures and the large sample size used for the area% measurement is assumed to account for the irregular shape of the phases. CALPHAD outputs predicted phase fractions in mol%; these predictions must be converted to vol% for comparison with the phase fraction measurements from electron microscopy. The unit cell volume and the number of atoms per unit cell of each phase was found in literature [23,33,34]. These were then used to calculate the molar volume, V_m, for each phase. The *vol%* of phase *i* could be calculated using the following equation.

$$vol\%_i = \frac{V_{m_i} * mol\%_i}{V_{tot}} \quad (1)$$

Where V_{m_i} is the molar volume of phase *i*, $mol\%_i$ is the predicted mol fraction of phase *i*, and V_{tot} is the total volume.

Samples for transmission electron microscopy (TEM) analysis were mechanically thinned to ~60 µm using a Fischione model 100 dimple grinder. Further thinning and perforation of TEM specimens was conducted using a Fischione model 1010 ion mill. Conventional TEM imaging and diffraction were performed using a FEI Tecnai TF20 microscope operating at an accelerating voltage of 200 keV. Atomic resolution high angle annular dark field (HAADF) scanning transmission electron microscopy (STEM) was carried out on a Thermo Scientific probe-corrected Themis Z S/TEM microscope operating at 300 keV.

CALPHAD simulations was done using Pandat software [35] and PanMg 2021a database which was updated for Mg-Zn-Y-Gd quaternary system. Since the focus of this work was on the Mg-rich region of this and this quaternary system and all constituent binary systems have been well established, thermodynamic models for the ternary systems (Mg-Zn-Gd, Mg-Zn-Y, and Mg-Gd-Y) were not updated. Validations show that the current thermodynamic descriptions for the Mg-Zn-Gd [36] and Mg-Gd-Y [37] ternary systems provide reasonable predictions. The previous thermodynamic description of Mg-Zn-Y ternary system was based on the experimental data of Refs. [38,39]. Recently, new experimental results and thermodynamic modeling were published for the Mg-Y-Zn ternary system [40,41]. Thermodynamic modeling from Xu et al. [40] is a general thermodynamic model for all LPSO phase polytypes and described the phase as $Mg_x(E_s, Mg)_6(E_l, Mg)_8$. In this model, E_s and E_l are elements with smaller and larger atomic radii than Mg, respectively. The LPSO polytype can be set based on the value of x. Since the number of Mg layers present between the RE and TM enriched layers is different for each polytype (e.g. three Mg layers in 14H and two layers in 18R), the number of Mg atoms in the structure (x) can be used to differentiate these polytypes. In addition, the general model presented by Xu et al. [40] also extended the homogeneity range of each element in the phase. Ruan et al. [41] also published new phase-equilibrium data of the Mg-Zn-Y ternary system. Their experimental data are comparable to those in Ref. [40] and used in the current work for thermodynamic optimization. In the present work, the solubility range of LPSO 14H is introduced using a model of $Mg_{70}(Mg,Gd,Y)_8(Mg,Zn)_6$, which is similar to the model used in [40]. The improved thermodynamic description is not only in agreement with the experimental data used in [38,39], but also agree well with the new experimental results in [40,41].

The preliminary description of the Mg-Zn-Y-Gd quaternary system is then obtained via extrapolation. However, calculations using this extrapolated quaternary database cannot well describe the experimental data obtained in the current work

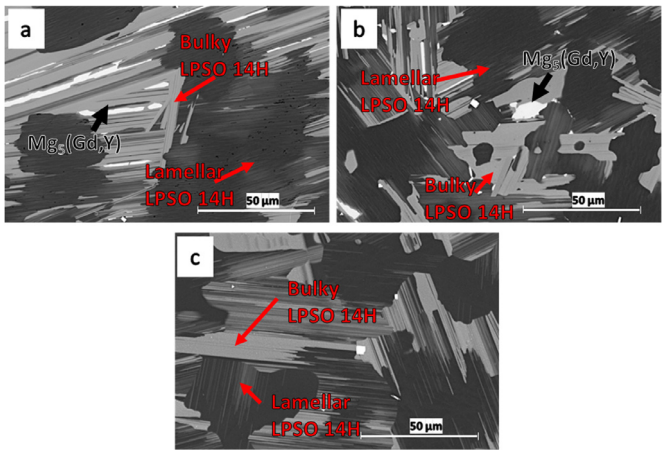

Fig. 2. SEM backscatter electron images of the Mg10Gd5Y3Zn composition in the (a) as cast, (b) solution treated at 400 °C 24 h, and solution treated at 500 °C 24 h conditions. Examples of the blocky and lamellar LPSO phase are labeled with red arrows and $Mg_5(Gd,Y)$ are labelled with black arrows (For interpretation of the references to color in this figure legend, the reader is referred to the web version of this article).

for the Mg-Zn-Y-Gd quaternary alloys. Further optimization is then performed on this preliminary description on the basis of the key experimental data of the current work.

3. Results and discussion

3.1. Microstructure

SEM analysis of the Mg10Gd4Y3Zn samples can be seen in Fig. 1. Three phases can be observed in the three conditions (as-cast, heat-treated at 400 and 500 °C): a dark matrix phase, a medium gray blocky phase at the grain boundaries, and a small bright cuboidal phase. A fine lamellar phase is also observed in the matrix. Based on EDS analysis, the dark matrix phase is the α-Mg matrix. The medium gray phase at the grain boundaries and the fine lamellar phase in the grains are consistent with an LPSO phase (indicated by red arrows in Fig. 1). The bright cuboidal phase is stable in all three conditions and does not exhibit a morphological change at the ST temperatures. Based on this observation and the EDS results with strong O, Gd, and Y signals, the cuboidal phase is assumed to be a RE-rich oxide (marked by yellow arrows) formed during casting. As a result, this phase is not considered with the present CALPHAD predictions. There is generally little change between the as-cast (Fig. 1a) and ST conditions (Fig. 1b and c), with the exception of an increase and thickening of the fine lamellar LPSO 14H observed in the matrix in the ST samples.

In the Mg10Gd5Y3Zn samples (Fig. 2), an additional phase can be observed in the as-cast and 400 °C samples. In the as-cast state (Fig. 2a), this additional phase is blocky and located interspersed in the blocky LPSO 14H phase. In the sample ST for 24 h at 400 °C (Fig. 2b), the morphology becomes more globular and the phase fraction is reduced. After ST at 500 °C for 24 h (Fig. 2c), this phase is no longer observed. Based on EDS analysis, the Mg:RE ratio was ~5:1 (at%), indicating this phase is consistent with $Mg_5(Gd,Y)$. This is further supported by its transformation into the LPSO 14H phase during ST at 500 °C, based on the CALPHAD results presented below. As with the Mg10Gd4Y3Zn sample, there was also an increase in phase fraction and thickening of the lamellar LPSO 14H in the matrix with ST.

The higher Zn-content alloy, Mg10Gd5Y5Zn, also exhibited a bright phase in addition to the α-Mg matrix, LPSO 14H, and RE-rich oxide phase (Fig. 3). The LPSO 14H phase in the Mg10Gd5Y5Zn alloy was further characterized using TEM and STEM. Fig. 4a and b are low magnification and atomic resolution HAADF-STEM images, respectively, of the LPSO 14H phase within the magnesium matrix. Fig. 4c and d are low magnification and atomic resolution HAADF-STEM images, respectively, of the bulk LPSO 14H phase. The RE-rich phase has a fish-bone like morphology that is different from the $Mg_5(Gd,Y)$ phase observed in the Mg10Gd5Y3Zn samples. In the as-cast condition (Fig. 3a), this bright phase is found either in contact with or in gaps between the LPSO 14H phase. EDS analysis suggests the Mg:Y:Zn ratio as ~3:2:3 (at%). The morphology and composition are consistent with the W-phase (reported by Luo et al. as $Mg_{31}Zn_{45}Gd_{24}$, at%) [14].

Fig. 5 shows the characterization of the W-phase in the as-cast Mg10Gd5Y5Zn alloy using TEM/STEM imaging. Fig. 5a is a bright field TEM image of the W-phase, with its corresponding selected area diffraction along [111] zone axis given in Fig. 5b. The lattice parameter of the W-phase measured using the electron diffraction pattern is about 0.708 nm, which is close to the value (0.6848 nm) previously reported for W-phase [25]. Figs. 5c and d are HAADF-STEM images of the W-phase at low magnification and atomic resolution, respectively. The chemical composition of the W-phase was measured using EDS in STEM mode and the result was inserted in Fig. 5c. A previous study indicated that Y and Gd could substitute for each other in the W-phase [42]. The atomic ratio of Mg, (Gd,Y) and Zn in Mg10Gd5Y5Zn is close to 3:2:3, which is consistent with the previously reported stoichiometry for W-phase [42,43]. Thus, the phase observed in this work is W-phase ($Mg_3Y_2Zn_3$) and not Mg_3RE as reported in some studies [14,44].

With ST of the alloy samples at 500 °C for 24 h (Fig. 3c), the W-phase fraction decreases and the phase morphology becomes more globular and disconnected. With the ST at 400 °C for 24 h (Fig. 3b), there is no obvious change in the W-phase morphology or phase fraction in comparison to the as-cast state. Equilibrium calculations, shown in Table 2, indicated that the W-phase should show a reduction in phase fraction at 400 °C, similar to the observations at 500 °C. This indicates that the kinetics of the W-phase dissolution may be slow at 400 °C or the phase is more stable than expected. To further investigate these hypotheses, an additional two stage ST of 500 °C for 24 h was conducted and followed by 400 °C for 24 h (Fig. 3d). With the two-stage ST, the reduction in W-phase fraction and morphology change observed in the 500 °C for 24 h sample was evident again. This supports the hypoth-

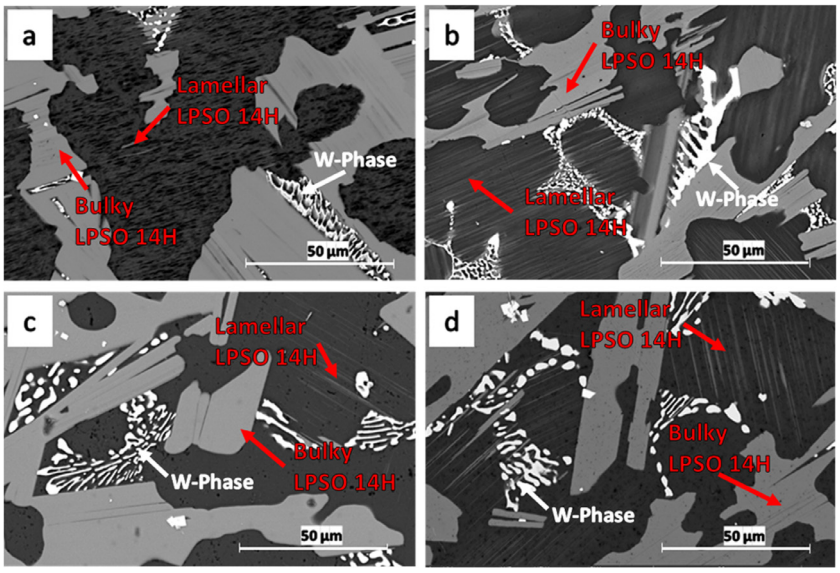

Fig. 3. SEM backscatter electron images of the Mg10Gd5Y5Zn composition in the (a) as cast, (b) solution treated at 400 °C 24 h, (c) solution treated at 500 °C 24 h, and (d) two-stage solution treated at 500 °C 24 h followed by 400 °C 24 h conditions. Examples of the blocky and lamellar LPSO phase are labeled with red arrows and W-phase are labelled with black arrows (For interpretation of the references to color in this figure legend, the reader is referred to the web version of this article).

Table 2
CALPHAD modeling phase fractions of Mg-Zn-Y-Gd alloys under Scheil and equilibrium conditions.

Alloy	Scheil			Equilibrium at 500 °C			Equilibrium at 400 °C		
	14H (vol%)	W (vol%)	$Mg_5(Gd,Y)$ (vol%)	14H (vol%)	W (vol%)	$Mg_5(Gd,Y)$ (vol%)	14H (vol%)	W (vol%)	$Mg_5(Gd,Y)$ (vol%)
Mg10Gd4Y3Zn	22.8	0	2.3	24.5	0	0	25.1	0	0
Mg10Gd5Y3Zn	19.8	0	4.7	21.5	0	0	21.8	0	2.0
Mg10Gd5Y5Zn	26.2	1.6	1.4	35.7	0.6	0	36.8	0.5	0

Table 3
Experimental phase fraction measurements Mg-Zn-Y-Gd alloys under as-cast and heat-treated conditions.

Alloy	As-cast			Heat treatment:500 °C, 24 h			Heat treatment:400 °C 24 h		
	14H (vol%)	W (vol%)	$Mg_5(Gd,Y)$ (vol%)	14H (vol%)	W (vol%)	$Mg_5(Gd,Y)$ (vol%)	14H (vol%)	W (vol%)	$Mg_5(Gd,Y)$ (vol%)
Mg10Gd4Y3Zn	32.7	0	0	30.2	0	0	30.1	0	0
Mg10Gd5Y3Zn	24.1	0	1.7	22.5	0	0	25.0	0	1
Mg10Gd5Y5Zn	42.4	2.0	0	43.9	1.6	0	44.7	2.8	0

esis that the W-phase is less stable at 400 °C, but that the dissolution kinetics are slower at 400 °C than at 500 °C. Once again, ST also increased the phase fraction and thickened the lamellar LPSO 14H in the matrix.

3.2. Phase fraction measurements and CALPHAD modeling

Table 3 shows the experimentally measured phase fractions to be compared with Pandat predictions (Table 2) of the three investigated alloys under different conditions. See the Experimental and Simulation Methods section for further discussion of phase fraction unit comparison and conversion.

Scheil simulations are often used to represent the solidification of alloys and to predict the phases in the as-cast microstructure [39]. In this work, the Scheil simulation results show that the $Mg_5(Gd,Y)$ phase is expected to form in all three alloys, while it was only experimentally observed in the as-cast microstructure of the Mg10Gd5Y3Zn alloy. This is likely due to fact that solid-state diffusion did occur during the casting process of these alloys, as opposed to the Scheil assumption of no solid-state diffusion. Such diffusion promotes the formation a large amount of 14H phase, suppressing $Mg_5(Gd,Y)$ phase. Therefore, there is insufficient RE accumulated at the end of solidification to form the $Mg_5(Gd,Y)$ phase for Mg10Gd4Y3Zn and Mg10Gd5Y5Zn alloys. The experimentally observed $Mg_5(Gd,Y)$ phase in Mg10Gd5Y3Zn alloy is also less than Scheil simulated results.

In our previous work, the LPSO 14H phase in the Mg-Zn-Y-Gd system was modeled as a line compound with a composition of $Mg_{70}(Y,Gd)_8Zn_6$ based on the crystal structure

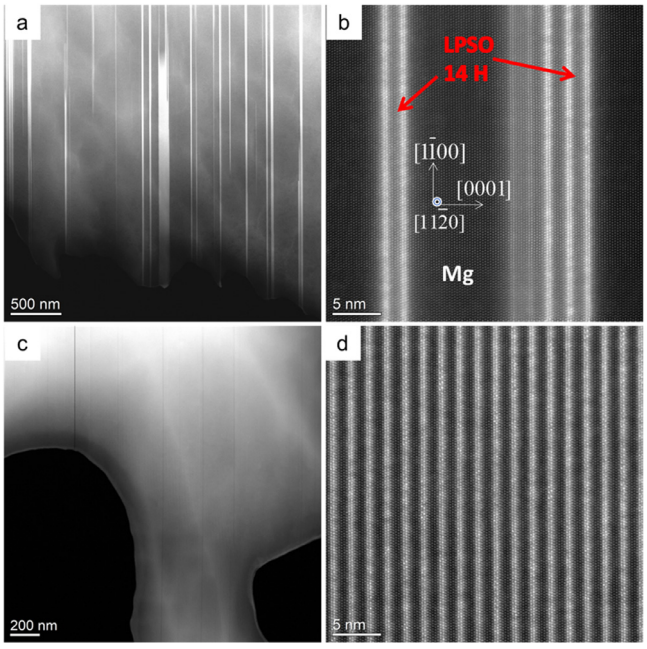

Fig. 4. STEM characterization of LPSO 14H phase in the as-cast microstructure of alloy Mg10Gd5Y5Zn: (a) low magnification and (b) atomic resolution HAADF-STEM image of LPSO 14H phase in magnesium matrix, (c) low magnification and (d) atomic resolution HAADF-STEM image of bulk LPSO 14H phase. LPSO 14H phase is present as a fine lamellar phase in the matrix and a blocky phase at the grain boundaries.

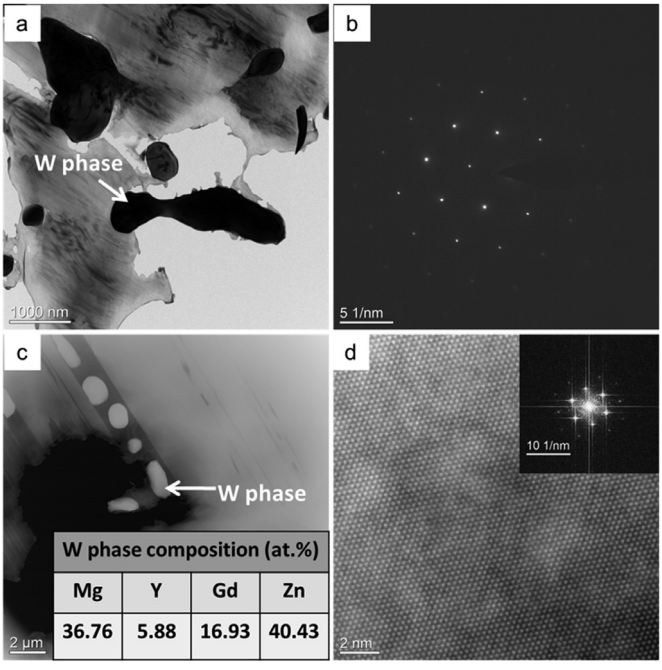

W phase composition (at.%)			
Mg	Y	Gd	Zn
36.76	5.88	16.93	40.43

Fig. 5. Characterization of the W-phase ($Mg_3Y_2Zn_3$) in the as-cast Mg10Gd5Y5Zn alloy: (a) bright field TEM image, (b) selected area diffraction along [111] zone axis of the W-phase, (c) HAADF-STEM image of W-phase with the inserted EDS composition measurement of the W-phase, and (d) atomic resolution HAADF-STEM image of the W-phase.

of the phase. This phase was a stoichiometric phase in the Mg-Zn-Y and Mg-Zn-Gd ternary sub-systems. The predicted phase fractions for LPSO 14H were considerably lower (~20 mol%) than the measured fractions [31]. In the present work, the LPSO 14H phase is modeled as $Mg_{70}(Mg,Y,Gd)_8(Mg,Zn)_6$ with some solid solubility range based on recently published experimental results [40,41]. As a result, the stable composition of LPSO 14H phase in both ternary systems are slightly shifted from the stoichiometric composition of $Mg_{70}M_8Zn_6$ (M = Y or Gd). The calculated results from the improved modeling agree better not only with the experimental data in literature [40,41], but also the experimental results in this work.

Fig. 6 represents the phase fraction vs temperature relationships of the three alloys under equilibrium condition based on the improved phase descriptions and model calibration. The calculated phase relationships agree well with the experimental results under different heat treatment conditions. For Mg10Gd4Y3Zn alloy (Fig. 6a), only (Mg) and 14H phases are stable from 350 °C to solidus temperature, which is supported by the microstructure of the as-cast sample, 400 and 500 °C heat treated samples. For Mg10Gd5Y3Zn alloy (Fig. 6b), which contains about 1.5 wt.% Y more than Mg10Gd4Y3Zn, the $Mg_5(Gd,Y)$ phase appears as a stable phase when the temperature is lower than 426 °C, and only (Mg) + 14H are stable phases at 500 °C. In the experimental results, the $Mg_5(Gd,Y)$ phase in the as-cast sample and 400 °C heat treated samples but is not observed in the 500 °C heat treated sample. It should be noted that $Mg_5(Gd,Y)$ is predicted for the Scheil model but is not observed in the as-cast samples. It is likely that slower cooling during casting resulted in enough diffusion in the solid which deviates from the Scheil conditions. Therefore, not all the predicted phases may be present in the as-cast exists condition. Beside the (Mg) and LSPO 14H phases, the W-phase is predicted as a stable phase with a small phase fraction in Mg10Gd5Y5Zn alloy as shown in Fig. 6c, which is consistent with the experimental observation of the W-phase being present in all Mg10Gd5Y5Zn samples after different heat treatments. The calculated phase fractions of the three alloys at different temperatures are in fairly good agreement with experimental observations. These results are on average only 5 mol% less than the experimental results according to Eq. (1).

In order to explore the impact of Y and Zn contents in Mg-Zn-Y-Gd alloys with high Gd content, two vertical sections of Mg-10Gd-5Y-xZn and Mg-10Gd-3Zn-xY have also been calculated as shown in Fig. 7. For Mg-10Gd-5Y-xZn alloys, when the Zn content is increased from 0 to about 5 wt.%, the (Mg) + 14 H two-phase region expands at elevated temperatures, and the W-phase becomes stable in the alloys with Zn content higher than 5 wt.%. According to the calculation for Mg-10Gd-3Zn-xY alloys, not only the stability of 14H phase is affected by the intermixing of Gd and Y on specific sublattice but also the stability of W-phase. The W-phase becomes more stable than LPSO 14H phase in the composition range of 0.5 wt.% $< Y <$ 1.5 wt.%, either of which is being in equilibrium with (Mg) phase. The LPSO 14H phase is sepa-

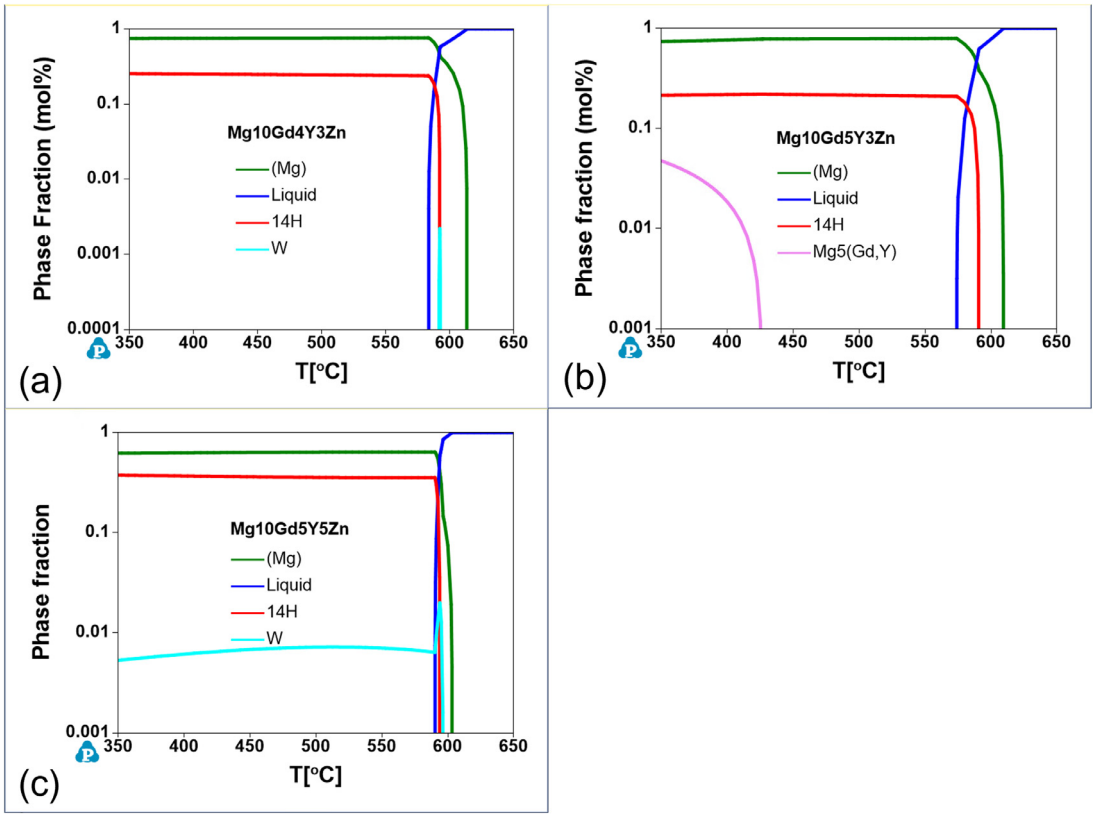

Fig. 6. Predicted equilibrium mole fraction vs. temperature for the three investigated alloys: (a) Mg10Gd4Y3Zn; (b) Mg10Gd5Y3Zn; and (c) Mg10Gd5Y5Zn.

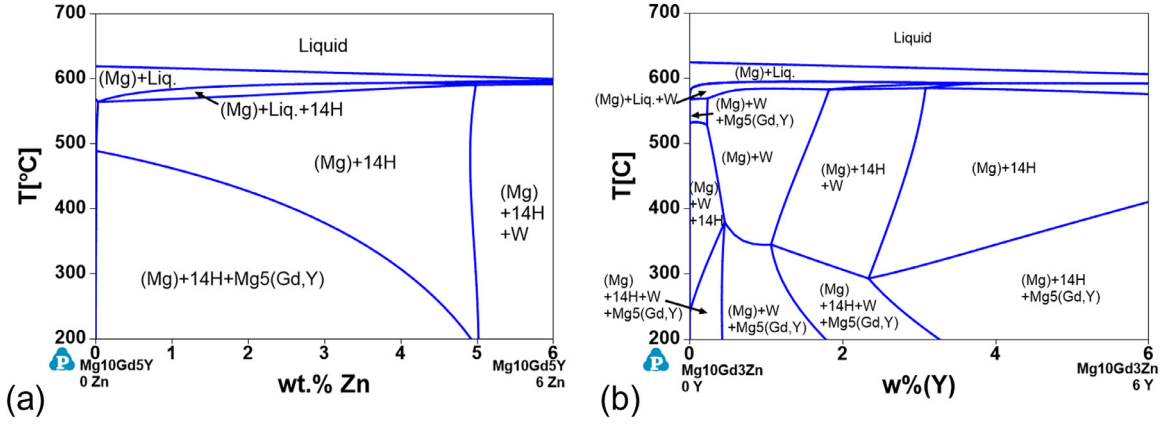

Fig. 7. Vertical sections of Mg-Gd-Y-Zn system: (a) Mg-10Gd-5Y-xZn; and (b) Mg-10Gd-3Zn-xY.

rated into two discontinuous regions, Gd-rich LPSO 14H (the atomic percentage of Y is close to zero) when $Y < 0.5$ wt.% and Gd and Y intermixing LPSO 14H (the atomic percentages of Gd and Y are close to equal) when $Y > 1.5$ wt.%. The $Mg_5(Gd,Y)$ phase is always stable at temperature lower than 300 °C.

4. Conclusions

Microstructural analysis and CALPHAD modeling were used to quantitatively understand the phase equilibria of three Mg-Gd-Y-Zn alloys in as-cast and solution treatment (ST) conditions. All three alloys were primarily composed of the Mg matrix and LPSO 14H phase. The lamellar LPSO 14H was found to thicken and increase in volume fraction with ST in each alloy. In the Mg10Gd5Y3Zn alloy, the $Mg_5(Gd,Y)$ phase was also observed in the as-cast and 400 °C conditions but is not stable at 500 °C. In the Mg10Gd5Y5Zn alloy, a fishbone-like RE-rich phase was observed. This RE-rich phase was identified using TEM/STEM analysis as the W-phase and not the Mg_3RE. ST of this alloy demonstrated that the phase fraction of the W-phase was reduced at 500 and 400 °C but does not completely transform. Based on these results, the thermodynamic models in Pandat database have

been improved to provide more accurate phase predictions for the important Mg-Gd-Y-Zn system. Specifically, there was a significant improvement in the quantitative LPSO 14H phase predictions due to model improvement, which is within an average of 5 mol% of experimental results.

Acknowledgements

This work was partially funded by the Army Research Laboratory (ARL) and Terves LLC. The authors would like to acknowledge Dr. Vincent Hammond with ARL, Dr. William Meier of Oak Ridge National Laboratory, and the members of Lightweight Materials and Manufacturing Laboratory at The Ohio State University (OSU) for their insightful discussions. This material is based upon work supported by the Army Contracting Command - Adelphi, MD under Contract No W911QX-18-P-0038. Any opinions, findings and conclusions or recommendations expressed in this material are those of the author(s) and do not necessarily reflect the views of ARL.

References

[1] J.F. Nie, Metall. Mater. Trans. A Phys. Metall. Mater. Sci. 43 (2012) 3891–3939, doi:10.1007/s11661-012-1217-2.
[2] F. Pan, M. Yang, X. Chen, J. Mater. Sci. Technol. 32 (2016) 1211–1221, doi:10.1016/j.jmst.2016.07.001.
[3] E. Abe, Y. Kawamura, K. Hayashi, A. Inoue, Acta Mater. 50 (2002) 3845–3857, doi:10.1016/S1359-6454(02)00191-X.
[4] C. Xu, G.H. Fan, T. Nakata, X. Liang, Y.Q. Chi, X.G. Qiao, G.J. Cao, T.T. Zhang, M. Huang, K.S. Miao, M.Y. Zheng, S. Kamado, H.L. Xie, Metall. Mater. Trans. A Phys. Metall. Mater. Sci. 49 (2018) 1931–1947, doi:10.1007/s11661-018-4507-5.
[5] D. Xu, E.H. Han, Y. Xu, Prog. Nat. Sci. Mater. Int. 26 (2016) 117–128, doi:10.1016/j.pnsc.2016.03.006.
[6] K. Kishida, K. Nagai, A. Matsumoto, A. Yasuhara, H. Inui, Acta Mater. 99 (2015) 228–239, doi:10.1016/j.actamat.2015.08.004.
[7] J.K. Kim, L. Jin, S. Sandlöbes, D. Raabe, Sci. Rep. 7 (2017) 1–8, doi:10.1038/s41598-017-04343-y.
[8] F. Lu, A. Ma, J. Jiang, D. Yang, Q. Zhou, Rare Met. 31 (2012) 303–310, doi:10.1007/s12598-012-0510-y.
[9] K. Wang, J. Wang, S. Huang, S. Gao, S. Guo, S. Liu, X. Chen, F. Pan, Mater. Sci. Eng. A 733 (2018) 267–275, doi:10.1016/j.msea.2018.07.050.
[10] S. Zhang, G.Y. Yuan, C. Lu, W.J. Ding, J. Alloy. Compd. 509 (2011) 3515–3521, doi:10.1016/j.jallcom.2010.12.136.
[11] T. Honma, T. Ohkubo, S. Kamado, K. Hono, Acta Mater. 55 (2007) 4137–4150, doi:10.1016/j.actamat.2007.02.036.
[12] K. Yamada, Y. Okubo, M. Shiono, H. Watanabe, S. Kamado, Y. Kojima, Mater. Trans. 47 (2006) 1066–1070, doi:10.2320/matertrans.47.1066.
[13] F. Shi, C. Wang, X. Guo, Rare Met. Mater. Eng. 44 (2015) 1617–1622, doi:10.1016/s1875-5372(15)30103-x.
[14] L. Luo, Y. Liu, M. Duan, Materials 11 (2018) 1351 (Basel), doi:10.3390/ma11081351.
[15] Y. Hu, C. Zhang, T. Zheng, F. Pan, A. Tang, Materials 11 (2018) (1942) (Basel), doi:10.3390/ma11101942.
[16] M. Yamasaki, M. Sasaki, M. Nishijima, K. Hiraga, Y. Kawamura, Acta Mater. 55 (2007) 6798–6805, doi:10.1016/j.actamat.2007.08.033.
[17] B. Li, B.G. Teng, D.G. Luo, Acta Metall. Sin. 31 (2018) 1009–1018 (English Lett., doi:10.1007/s40195-018-0769-6.
[18] G. Garces, P. Pérez, R. Barea, J. Medina, A. Stark, N. Schell, P. Adeva, Metals 9 (2019) 221 (Basel), doi:10.3390/met9020221.
[19] M. Nishijima, K. Hiraga, M. Yamasaki, Y. Kawamura, Mater. Trans. 47 (2006) 2109–2112, doi:10.2320/matertrans.47.2109.
[20] A. Issa, J.E. Saal, C. Wolverton, Acta Mater. 83 (2015) 75–83, doi:10.1016/j.actamat.2014.09.024.
[21] J. Zhang, S. Liu, R. Wu, L. Hou, M. Zhang, J. Magnes. Alloy. 6 (2018) 277–291, doi:10.1016/j.jma.2018.08.001.
[22] P. Manfrinetti, K.A. Gschneidner, J. Less Common Met. 123 (1986) 267–275, doi:10.1016/0022-5088(86)90135-9.
[23] M. Sahlberg, Y. Andersson, J. Alloy. Compd. 446–447 (2007) 134–137, doi:10.1016/j.jallcom.2006.12.086.
[24] J. Gröbner, A. Kozlov, X.Y. Fang, S. Zhu, J.F. Nie, M.A. Gibson, R. Schmid-Fetzer, Acta Mater. 90 (2015) 400–416, doi:10.1016/j.actamat.2015.02.044.
[25] Z.P. Luo, H. Hashimoto, Micron 31 (2000) 487–492, doi:10.1016/S0968-4328(99)00128-6.
[26] H.S. Jiang, X.G. Qiao, C. Xu, M.Y. Zheng, K. Wu, S. Kamado, Mater. Des. 108 (2016) 391–399, doi:10.1016/j.matdes.2016.06.116.
[27] S. Zhong Wu, J. Shan Zhang, C. Xiang Xu, K. Bo Nie, X. Feng Niu, Z. Yong You, China Foundry 14 (2017) 34–38, doi:10.1007/s41230-017-5074-x.
[28] Q. Chen, A. Tang, J. Ye, L. Hao, Y. Wang, T. Zhang, Mater. Sci. Eng. A 686 (2017) 26–33, doi:10.1016/j.msea.2017.01.012.
[29] F. Shi, C.Q. Wang, Z.M. Zhang, Trans. Nonferr. Met. Soc. China 25 (2015) 2172–2180 (English Ed, doi:10.1016/S1003-6326(15)63829-8.
[30] B. Li, K. Guan, Q. Yang, X. Niu, D. Zhang, Z. Yu, X. Zhang, Z. Tang, J. Meng, J. Alloy. Compd. 763 (2018) 120–133, doi:10.1016/j.jallcom.2018.05.308.
[31] J.M. Meier, J. Caris, A.A. Luo, in: Magnesium Technology, Springer International Publishing, San Diego, CA, 2020, pp. 61–69, doi:10.1007/978-3-030-36647-6.
[32] M.A. Delesse, Procédé Mécanique Pour Déterminer La Composition Des Roches, F. Savy, Paris, 1866.
[33] D. Egusa, E. Abe, Acta Mater. 60 (2012) 166–178, doi:10.1016/j.actamat.2011.09.030.
[34] M.L. Fornasini, P. Manfrinetti, K.A. Gschneidner, Acta Crystallogr. Sect. C Cryst. Struct. Commun. 42 (1986) 138–141, doi:10.1107/s0108270186097019.
[35] W. Cao, S. Chen, F. Zhang, K. Wu, Y. Yang, Y.A. Chang, R. Schmid-fetzer, W.A. Oates, CALPHAD Comput. 33 (2009) 328–342 Coupling Phase Diagrams\penalty \z@ \protect \futurelet\@let@token Thermochem, doi:10.1016/j.calphad.2008.08.004.
[36] J. Gröbner, A. Kozlov, X.Y. Fang, S. Zhu, J.F. Nie, M.A. Gibson, R. Schmid-Fetzer, Acta Mater. 90 (2015) 400–416, doi:10.1016/j.actamat.2015.02.044.
[37] J. Gröbner, R. Schmid-Fetzer, Scr. Mater. 63 (2010) 674–679, doi:10.1016/j.scriptamat.2010.01.035.
[38] J. Gröbner, A. Kozlov, X.Y. Fang, J. Geng, J.F. Nie, R. Schmid-Fetzer, Acta Mater. 60 (2012) 5948–5962, doi:10.1016/j.actamat.2012.05.035.
[39] R. Schmid-Fetzer, J. Groebner, M. Yamasaki, Y. Kawamura, H. Okuda, S. Miura, T. Horiuchi, J.-F. Nie: Thermal stability of Mg-Zn-Y LPSO Phases and Revised Thermodynamic Description of the Mg-Zn-Y Phase Diagram. Mg 2015-The 10th International Conference on Magnesium Alloys and Their Applications. October 11-16, 2015, Jeju, Korea. Symp. LPSO Structure & Its Related Alloys, Invited, October 12, 2015. eProceedings, EO-3-0372, pp 1–23.
[40] K. Xu, S. Liu, K. Chang, Y. Liang, Y. Du, Z. Jin, J. Magnes. Alloy. 9 (2021) 144–155, doi:10.1016/j.jma.2019.12.008.
[41] Y. Ruan, C. Li, Y. Ren, X. Wu, R. Schmid-Fetzer, C. Guo, Z. Du, J. Mater. Sci. Technol. 68 (2021) 147–159, doi:10.1016/j.jmst.2020.08.019.
[42] Y. Liu, G. Yuan, C. Lu, W. Ding, Scr. Mater. 55 (2006) 919–922, doi:10.1016/j.scriptamat.2006.07.035.
[43] H. Yan, R.S. Chen, E.H. Han, Mater. Sci. Eng. A 527 (2010) 3317–3322, doi:10.1016/j.msea.2010.02.038.
[44] S. Zhang, G.Y. Yuan, C. Lu, W.J. Ding, J. Alloy. Compd. 509 (2011) 3515–3521, doi:10.1016/j.jallcom.2010.12.136.